

Effect of Disk-to-Disk Variations on the Nonlinear Static Characteristics and Stability Regimes of Coned Disk Spring Stacks: Experimental and Computational Studies of Quasi-Zero-Stiffness Isolators

Paul Gilmore, Umesh Gandhi

Toyota Research Institute of North America

Rajendra Singh

Department of Mechanical & Aerospace Engineering, The Ohio State University

In this study, we introduce a novel approach to creating a Quasi-Zero Stiffness (QZS) isolator utilizing off-the-shelf coned disk springs with a unique stack. These springs are affordable, compact, and can be adapted for a broad spectrum of force requirements, enabling the achievement of the QZS effect using a solitary component, thereby eliminating the need to balance between positive and negative stiffness elements. To address the issue of the limited displacement range offered by a single coned spring, the solution involves layering multiple disk springs with rigid spacers. Nonetheless, the nonlinear force-deflection behavior is significantly affected by manufacturing-driven geometric variability due to inherent differences from one disk spring to another. This aspect of variability has been overlooked by previous researchers, who have operated under the assumption that all disks in a stack are identical. This research delves into how variations in the disk springs' geometry impact the nonlinear static behavior of the QZS stacks, employing both experimental and computational techniques. We illustrate the stability conditions and pinpoint the occurrences of buckling and snap-through events. Computational model for the multi-disk engineered stack is experimentally validated. Finally, we explore the QZS isolator design approaches that would take into account these geometric variations.

1. Introduction

The chief motivation behind this article to employ coned disk stacks for use as quasi-zero stiffness (QZS) vibration isolators. Such coned disks (also known as the Beleville washers) are traditional machine elements that have been historically employed as preload devices in mechanisms, mechanical systems and civil engineering applications. Almen and Laszlo [1] analytically defined the load-deflection expression in 1936. Curti et al. [2-3] refined the analysis by introducing the Poisson's ratio term and validated the simple expressions by comparing the predicted load-deflection curves with empirical static measurements. Earlier work [1-3] remains the basis for further theoretical work. In particular, edge friction effects have received much attention [4-6] using analytical and experimental methods; see a recent article by Masticola et al. [5] for a comprehensive review of the coned disk literature.

In many applications, it may be desirable to not only reduce vibrations at a few critical frequencies but rather over broad frequency ranges and operating conditions [7]. New materials and structures for vibrations isolators and absorbers are needed to meet these requirements while seeking lower cost and reduced design complexity. The QZS structures are most promising

candidates for isolation over a wide frequency range while having good load-bearing capability and passive operation [8-13]. The concept for quasi-zero stiffness has been around for more than a decade, but recently many innovative QZS structures have been designed [9-21]. For instance, the geometric nonlinearity is a common technique used to obtain QZS property [9]. Scissor or x-shaped mechanisms with horizontal springs for negative stiffness are recent examples and have been shown to have large stroke and in-situ adjustable capability among other advantages [14-15]. Another method to achieve QZS or nonlinear stiffness is using deformable components. Most often, this is accomplished by beam flexure, and several novel designs have been explored [16-18]. The purely mechanical devices used to obtain the desired force-deflection characteristics usually have some drawbacks such as overall weight and size. The QZS structures using pneumatic and magnetic components and combinations have shown to have advantages of lightweight, non-contact, and easier adjustability [9-13,19-21].

In addition to quasi-zero stiffness behavior, design of mechanisms for achieving a certain prescribed force-deflection curve or other nonlinear stiffness behavior has been a popular topic recently. For example, an elastic beam with movable end constraint can be exploited to achieve complex force-deflection curves depending on the design parameters [22]. Also, a system with a pair of oblique springs could obtain variety of force-deflection characteristics [23]. Such types of structures may be useful in areas such as energy absorption, fast actuation, and deployable structures [14]. The large majority of these QZS and nonlinear stiffness mechanisms are conceptually based on a combination of negative stiffness element in parallel with a positive stiffness element. Recently, a few studies have addressed this challenge by having a single element which displays typical QZS behavior [24-25]. Such elements may have strong advantages with respect to minimizing size and complexity. Many practical applications often have limited space for installation, and it is important for isolators to be compact. Unfortunately, the negative stiffness element of QZS isolators often has a large footprint or height, and the whole isolator is ultimately much larger than the object it is intended to support. Thus, there is a need to develop more compact QZS vibration isolators from a practical standpoint.

Another challenge of many QZS isolators is the small working range of the QZS region, and the isolator is only effective for small input amplitudes. This problem has been recognized and has been the primary topic or sub-topic in several studies [12, 26-30]. Since larger displacements tend to occur at lower frequencies, a small working range may interfere with the intended purpose of QZS isolators to isolate at lower frequencies. Larger working range of the QZS region allows some of the undesirable non-linear dynamic phenomena to be avoided such as excitation amplitude dependence and jump phenomenon. Therefore, sufficient working range is a crucial design consideration.

To overcome the above-mentioned limitations and challenges, we propose a coned disk based QZS isolator. First, coned disks have highly nonlinear force-deflection regimes [1-5], and their stiffnesses can be positive, zero or negative depending on the geometry and material properties. Therefore, a QZS isolator may be theoretically constructed from a single coned disk, without separate positive and negative stiffness components. Second, coned disks have both small footprint and vertical height, which allows for very compact QZS isolators that can support large loads. Third, coned disks can be cascaded in several configuration as exhibited by Mastricola and Singh [31], including stacking in series to increase deflection. Stacking is an

efficient method to achieve any desired stroke for the QZS isolator without increasing the footprint.

Disk spring stacks have also been proposed previously as QZS isolators by Valeev et al. [32-33]. We extend their work by considering the engineering design aspects of such stacks; see [34] for an earlier effort. Our experimental studies show that the disk-to-disk variations significantly complicate the design and application of disk spring stacks. In particular, the manufacturing tolerances of disk springs can lead to seemingly unrepeatable and unpredictable stack behavior. The primary goal of this article is to understand how the variations in individual disk springs influence the nonlinear force-deflection behavior of an engineered stack.

2. Problem Formulation

A major assumption made in previous disk spring stack designs [31-33] is that every coned disk in the stack is identical, and therefore the deflections of each spring are always equal [32-34]. Then, a force-deflection relation for the stack can be easily developed based on the relation for a single disk spring by substituting δ/n for δ in relationship for a single disk spring, where δ is the static deflection and n is the number of disk elements. This method linearly scales the displacement by n . However, our experimental investigations have found this to be an inappropriate assumption in predicting the behavior in the QZS region due to significant disk-to-disk variations.

A single coned disk spring geometry is completely defined by its height h , thickness τ , inner diameter $2b$ and outer diameter $2a$ as defined in Figure 1a. Typical force-deflection curves for a few h/τ ratios are plotted in Figure 1b according to Equation 1, which is a previously developed analytical model where E is the Young's modulus, α is a/b , and δ is the deflection [5].

$$P(\delta) = \frac{E\delta\pi}{a^2} \left(\frac{\alpha}{\alpha-1} \right)^2 \left[(h - \delta) \left(h - \frac{\delta}{2} \right) M + N \right] \quad (1)$$

$$M = \left(\frac{\alpha+1}{\alpha-1} - \frac{2}{\ln(\alpha)} \right) \tau \quad (1.1)$$

$$N = \frac{\tau^3}{6} \ln \alpha \quad (1.2)$$

The above equation assumes that there is no edge friction between the spring and upper and lower boundaries, the loads are evenly distributed around the disk spring circumference, the disk spring angular rotation is small and small angle approximation can be used, radial stresses are negligible, and the cross section does not distort. The force is strongly sensitive to the h/τ ratio, and this is a well-known characteristic of conical disk springs.

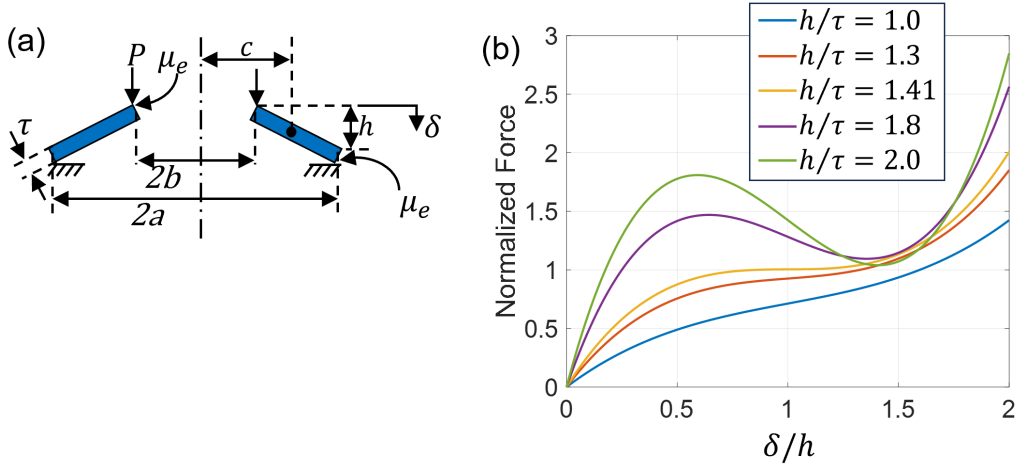


Figure 1: Schematic and load-deflections of typical coned disk springs: Geometry of single disk spring where τ is the thickness, b is the inner radius, a is the outer radius, h is the height, μ_e is the edge friction coefficient, P is the force, c is the point about which the cross section rotates, and δ is the displacement (a), and force-deflection dependence on selected h/τ ratios computed from Eqn. 1.

Our experimental studies reveal that typical disk-to-disk variations (due to manufacturing tolerances) can result in the h/τ ratio varying by as much as 21% from the nominal value, causing both the force and stiffness to have large variations. For example, when the nominal h/τ ratio is 1.41, the actual measured values reside between 1.25 and 1.57. Consequently, when these springs are stacked in series, it cannot be assumed that they maintain equal deflections. A wide variety of stack behavior are possible depending on the number of springs, h/τ ratios of the springs, and the magnitude of the h/τ ratio variation, as well as other assembly issues. In many cases, snap-through, multiple regime stability, and direction-dependence are observed, and behavior may appear unpredictable due to the disk-to-disk variations. This is indeed one of the major challenges to designing disk spring-based QZS isolators for engineering applications especially when off-the-shelf production parts must be used. It is therefore essential to develop a scientific understanding of the nonlinear behavior in order to successfully design QZS isolators based on such stacks. Accordingly, the main objectives of this article are to: (1) quantify the effect of disk-to-disk variations on the nature of the disk spring stacks via experimental means; (2) develop a computational model of a stack (with an arbitrary number of coned disks and spacers) which can account for such variations; (3) quantify the resulting nonlinear static behavior and multi-regimed stability maps of stacks consisting of 2, 3 or multiple disk elements, and (4) consider how to design practical disk spring-based QZS isolators given significant variations.

3. Design of Single Disk Spring and Identification of Relevant Disk-to-Disk Variations

3.1 Critical Design Factors

A disk spring can function as a QZS isolator by designing its stiffness to be zero the deflection midpoint (i.e., when $\delta = h$). Differentiate Eqn. 1 to get the analytical stiffness expression (Eqn. 2) and set it equal to zero.

$$\frac{\partial P}{\partial \delta}(\delta) = \frac{E\pi}{a^2} \left(\frac{\alpha}{\alpha-1} \right)^2 \left[\delta \left(\frac{1}{2}(\delta - h) + \left(\frac{\delta}{2} - h \right) \right) M + (h - \delta) \left(h - \frac{\delta}{2} \right) M + N \right] \quad (2)$$

$$\frac{\partial P}{\partial \delta}(h) = \frac{E\pi}{a^2} \left(\frac{\alpha}{\alpha-1} \right)^2 \left[h \left(-\frac{h}{2} \right) M + N \right] = 0 \quad (3)$$

$$\left(-\frac{h^2}{2} \right) \left(\frac{\alpha+1}{\alpha-1} - \frac{2}{\ln(\alpha)} \right) \tau + \frac{\tau^3}{6} \ln \alpha = 0 \quad (3.1)$$

$$\frac{h}{\tau} = \sqrt{\frac{(\alpha-1) \ln^2(\alpha)}{3(\ln(\alpha)(\alpha+1)-2(\alpha-1))}} \quad (3.2)$$

Then, we set $\delta = h$ in Eqn. 3 and rearrange to find that the ratio h/τ is very close to 1.41, or $\sqrt{2}$, for a wide range of α values (see Eqn. 3.2 plotted in Figure 2). Therefore, it is seen that QZS behavior can be achieved with a single component, avoiding the need to correctly balance negative and positive stiffness components in typical QZS isolators. Such conical disk springs have several benefits as QZS isolators including simple construction, low cost, small footprint, easily customizable to any QZS force level by keeping h/τ ratio constant and tuning thickness, outer diameter, and inner diameter.

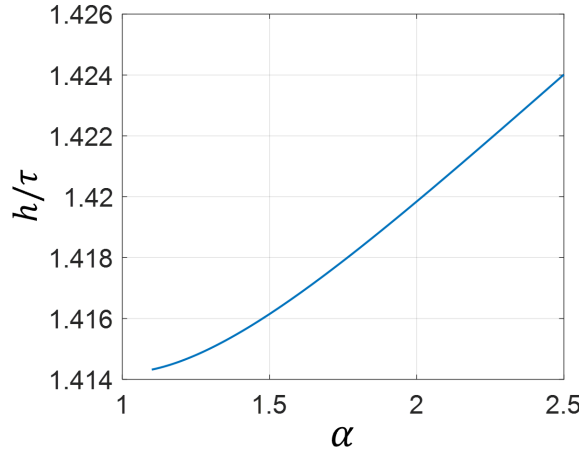


Figure 2: The h/τ ratio which results in zero stiffness at the deflection midpoint as a function of α .

In this paper, we rely on experimental methods first to observe the relevant effects of the variations. We choose a commercially available disk spring with nominal h/τ ratio close to 1.41 to be the focus of the study. It is made from steel and has the geometry listed in Table 1. Full stroke force deflection curves of both individual springs and stacks are obtained under displacement control. A cutoff force of 200 N is used during the forward stroke and then the displacement is reversed to obtain loading and unloading force-deflection curves. At 200 N, the disk springs are close to their fully inverted positions. The displacement rate is approximately 0.5 mm/s for all tests. One hundred (nominally similar) disk springs are randomly selected and measured. The average force as a function of deflection for the loading direction is plotted in Figure 3 with error bars of ± 1 standard deviation (STD).

Table 1: Nominal geometry of coned disk spring considered in this paper; see Figure 1 for the symbols.

Geometry	Nominal value [mm]
$2a$	34.5
$2b$	22.4
h	0.7
τ	0.5

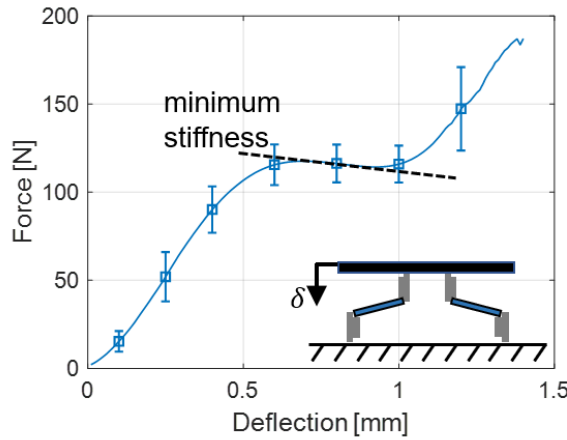


Figure 3: Measured average load-deflection curve of 100 randomly selected disk springs with +/- 1 standard deviation error bars and for the loading direction only.

Although this plot is useful to see how the force varies, it is also important to consider how the stiffness varies in the QZS region. The minimum stiffness, as depicted in Figure 3, is found for each spring and plotted in the histogram of Figure 4. The stiffness varies substantially, ranging from -100 N/mm to 20 N/mm with an average of -34 N/mm. Force-deflection curves for springs in the left, middle, and right regions of the histogram are additionally plotted in Figure 4 as well to visualize the stiffness variation within the QZS region. Such variations clearly pose a significant challenge in applying disk springs as QZS isolators even if the nominal geometry is designed correctly.

One of the implications of this result is that the majority of springs have a substantial negative stiffness in the QZS region, even though the disk spring with nominal geometry is not expected to have a negative stiffness. There are a few geometric parameters and physical properties which can affect the stiffness. The stiffness is proportional to the Young's modulus, but E would have to vary by >800% to result in the observed variation in stiffness. Also, a variation in the E values alone cannot cause the stiffness to change from negative to positive. Therefore, we do not expect a variation in the material properties to be a significant contributor to the stiffness variability.

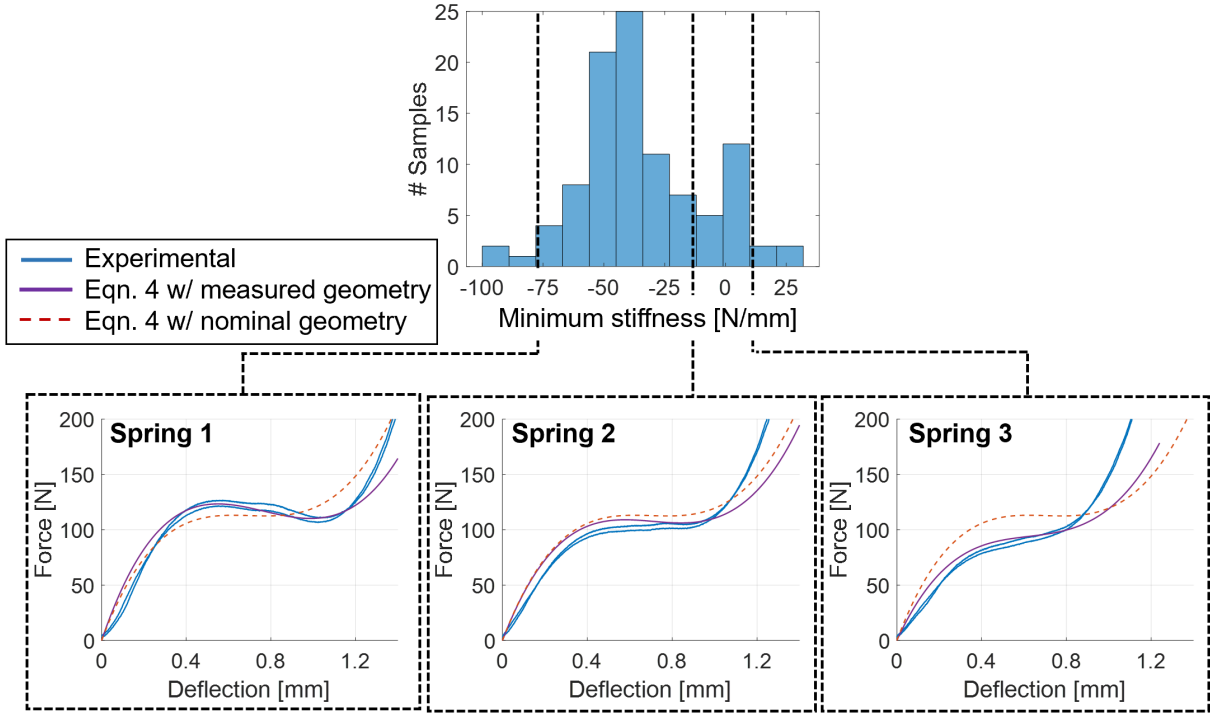


Figure 4: Histogram of minimum stiffnesses in the QZS region, from experimental force-deflection data of 100 randomly selected coned disk spring elements.

A second factor which may affect the stiffness is the edge friction coefficient. An extension of Equation 1 which accounts for edge friction is given by [5]

$$P(\delta) = \frac{\frac{E\delta\pi}{a^2} \left(\frac{\alpha}{\alpha-1} \right)^2 \left[(h-\delta) \left(h - \frac{\delta}{2} \right) \left(\frac{\alpha+1}{\alpha-1} - \frac{2}{\ln(\alpha)} \right) \tau + \frac{\tau^3}{6} \ln \alpha \right]}{1 - \left[\mu_e \frac{h-\delta+\tau}{a-b} \right] \text{sgn}(\delta)} \quad (4)$$

where μ_e is the edge friction coefficient. Figure 5 shows the loading direction force-deflection curves found using Eqn. 4 for different friction coefficients. The stiffness at the deflection midpoint is zero in the frictionless case and becomes negative as friction is introduced. When $\mu_e = 0.8$, the minimum stiffness is approximately -21 N/mm. Friction coefficients have to be > 1.5 to result in stiffnesses of -34 N/mm and below, which is out of the typical range for steel-to-steel interfaces. Also, the friction coefficient is unlikely to vary by such a large percentage from sample to sample. Moreover, friction only causes the stiffness to become more negative in the QZS region as seen from Figure 8 and it cannot cause it to become positive during the forward stroke. For these reasons, it is concluded that the edge friction is also not the primary cause of the stiffness variability.

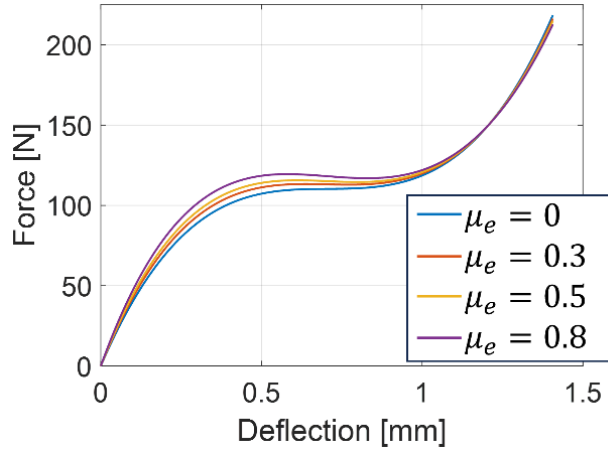


Figure 5: Effect of the edge friction coefficient on stiffness in the QZS region found using Equation (4) in the loading direction.

The third factor which can affect the stiffness is the geometric h/τ ratio, and it is most likely that variabilities in height and thickness are the primary cause of stiffness variability. To support this conclusion, we measured the heights of three typical springs from Figure 4 using a laser microscope (Keyence VK-X200), and the results are illustrated in Figure 6. The springs have heights of 0.77, 0.71, and 0.62 mm respectively. The thickness, inner diameter, and outer diameter of all three springs was also determined using digital calipers, and the precise geometries of each spring have been listed in Table 2. The experimentally determined h/τ ratios are 1.6, 1.5, and 1.29 respectively. Given that the stiffness in the QZS region should be positive for h/τ ratios less than 1.41 and increasingly negative for h/τ ratios greater than 1.41, these measured values can explain the stiffness variability. The exact spring geometries in Table 2 are substituted into Equation 4 with an assumed friction coefficient for steel-steel contact of 0.5, and the curves are plotted in Figure 4 with the experimental data. When the measured geometry is used in the analytical model, the calculation agreements with experimental data are much closer compared to when the nominal geometry is used.

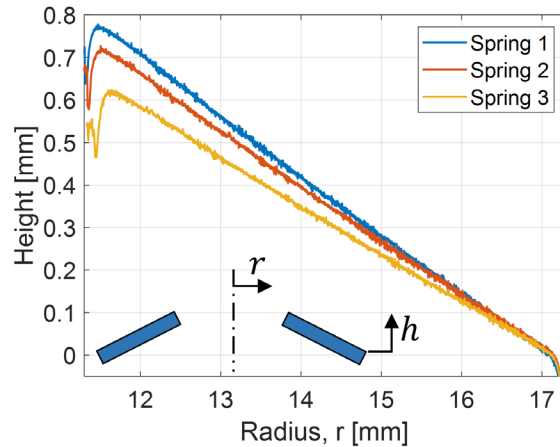


Figure 6: Measured heights of Spring 1, Spring 2, and Spring 3 from Figure 4.

Table 2: Precise geometries for Spring 1, Spring 2, and Spring 3 (of Figure 4) measured using laser microscope and digital calipers; nominal values are listed in Table 1.

	h [mm]	τ [mm]	$2a$ [mm]	$2b$ [mm]
Spring 1	0.77	0.49	34.3	22.6
Spring 2	0.71	0.49	34.3	22.6
Spring 3	0.62	0.49	34.4	22.5

One important conclusion from this experimental study is that it is difficult to neglect geometric tolerances when comparing disk spring models to experimental results due to the strong sensitivity of stiffness to the h/τ ratio. Furthermore, based on the results of Figure 6 and Table 2, we conclude that h is the primary contributor to the h/τ variability. By tuning h and keeping τ constant, the h/τ ratio may be varied from 1.30 to 1.78 to simulate the range of stiffness measured in Figure 4. Therefore, we explore the effect of the h/τ ratio on the engineered stack behavior in subsequent sections.

3.2 Examination of Coned Disks from Extreme Regions

Next, we specifically select six springs from the two extreme regions of the stiffness histogram and construct stacks. The stack design was a topic of our previous work [34]. It consists of disk springs separated by rigid inner and outer spacers as seen in Figure 7a, b. The spacers allow the springs to be compressed past the flat position to fully inverted position. In Stack A, a stack of 6 springs is constructed using springs toward the left region of the histogram (stiffnesses less than -65 N/mm). In Stack B, a stack of 6 springs is constructed using springs toward the right region of the histogram (stiffnesses > 0 N/mm). Measured loading and unloading curves for each stack are plotted in Figure 7c and 7d respectively. Clear differences are observed between Stack A and Stack B which highlight the impact of the disk-to-disk variations. First consider Stack A where the QZS region is characterized by successive buckling or snap-through of each individual disk. It is important to distinguish between classical buckling and “snap-through” behavior. Buckling is associated with negative stiffness regions where the load decreases over a certain displacement. On the other hand, snap-through is a dynamic event where the operating load suddenly jumps to a different value due to an instability. Both types of behavior can be seen in the Stack A force-deflection curve. Also, some springs do not necessarily snap back at the same position during loading and unloading. For example, during loading, a snap is observed at about 6.2 mm. During unloading, the first snap does not occur until about 5.8 mm. These shifts in the snap-through positions between loading and unloading demonstrate the directional dependence of the force-deflection properties. The implication of this directional dependence is a hysteresis in the QZS region that is not due to edge friction.

Conversely, no buckling events and no directional dependence are observed in Stack B. The stiffness is approximately constant (9.5 N/mm) throughout the QZS regime. The hysteresis in this stack is due only to edge friction but its contribution is minimal compared to the hysteresis from snap-through events, and therefore we choose to neglect it in the analytical modeling of disk spring stacks. These two examples demonstrate how variation in individual springs leads to significant differences in the nonlinear load-deflection characteristics of the

stacks, especially in the QZS region. A more robust engineering QZS isolator design approach that accounts for the variations is needed to successfully apply commercially available disk springs in the stacks.

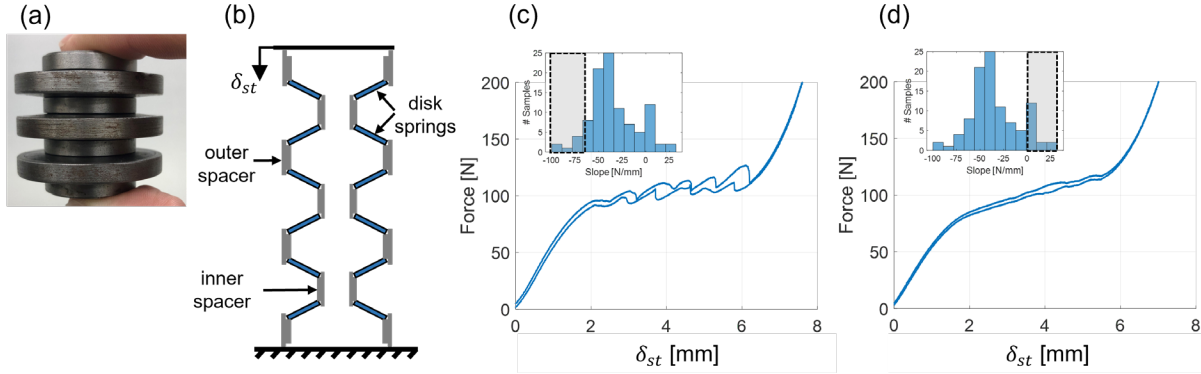


Figure 7: Image of disk spring stack with 6 springs and rigid spacers (a), schematic of disk spring stack (b), experimental force-deflection of stacks constructed from springs in left region of histogram resulting in Stack A (c), and right region of histogram leading to Stack B (d).

4. Development of an Analytical Model of Disk Spring Stack Given Disk-to-Disk Variations

4.1 Analysis of Two-Spring Stack

The geometry and variables of a two-spring stack under displacement control are shown in Figure 8. The springs have heights of h_1 and h_2 respectively, and the displacement input is δ_{st} . The springs are in series and therefore each must carry the same elastic force. The deflections of the springs can be expressed as a function of δ_{st} and δ_1 . For example, the deflection of the upper spring is $\delta_{st} - \delta_1$. Then, using Eqn. 1, we equate the force in spring 1 and spring 2 and simplify to get:

$$\frac{M}{2}(\delta_{st} - \delta_1)^3 - \frac{3h_2M}{2}(\delta_{st} - \delta_1)^2 + (h_2^2M + N)(\delta_{st} - \delta_1) = \frac{M}{2}(\delta_1)^3 - \frac{3h_1M}{2}(\delta_1)^2 + (h_1^2M + N)(\delta_1) \quad (5)$$

Then, the force in stack can be determined by Eqn. 6 where $\gamma = \frac{E\delta\pi}{a^2} \left(\frac{\alpha}{\alpha-1} \right)^2$.

$$F = \gamma \left[\frac{M}{2}(\delta_{st} - \delta_1)^3 - \frac{3h_2M}{2}(\delta_{st} - \delta_1)^2 + (h_2^2M + N)(\delta_{st} - \delta_1) \right] \quad (6)$$

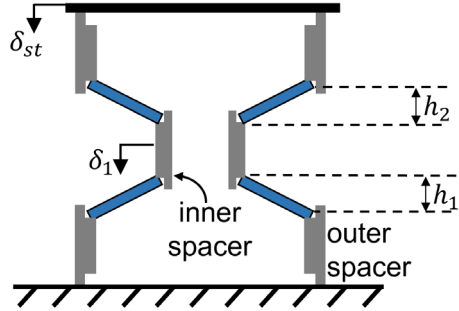


Figure 8: Model of 2-spring stack where each spring can have different height, and therefore different h/τ ratio. The input is δ_{st} and δ_1 is a displacement response coordinate.

Equation 5 has only one unknown variable, δ_1 , and can be directly solved using numerical methods, and the solutions are substituted into Equation 6 to determine the force for each δ_1 . Since Eqn. 5 is a cubic equation of δ_1 , up to three real solutions are possible. Re-cast Eqn. 5 in the standard form

$$A\delta_1^3 + B\delta_1^2 + C\delta_1 + D = 0 \quad (7)$$

then the discriminant can be calculated using:

$$\Delta = B^2C^2 - 4AC^3 - 4B^3D - 27A^2D^2 + 18ABCD \quad (8)$$

If $\Delta > 0$, then the system has three equilibrium points, and if $\Delta < 0$, the system has only one equilibrium point for a prescribed δ_{st} . The potential energy, U , of the system is the sum the potential energy of each spring:

$$U = \gamma \left[\left(\frac{M}{8} (\delta_{st} - \delta_1)^4 - \frac{h_2 M}{2} (\delta_{st} - \delta_1)^3 + \frac{h_2^2 M + N}{2} (\delta_{st} - \delta_1)^2 \right) + \left(\frac{M}{8} \delta_1^4 - \frac{h_1 M}{2} \delta_1^3 + \frac{h_1^2 M + N}{2} \delta_1^2 \right) \right] \quad (9)$$

Since δ_{st} is the input, the stability of a given equilibrium point $\{\delta_1\}$ can be determined by the second derivative of the potential energy with respect to δ_1 :

$$\frac{\partial^2 U}{\partial \delta_1^2} = \gamma \left[\frac{3M}{2} (\delta_{st} - \delta_1)^2 - 3h_2 M (\delta_{st} - \delta_1) + (h_2 M + N) + \frac{3M}{2} \delta_1^2 - 3h_1 M \delta_1 + h_1^2 M + N \right] \quad (10)$$

The solution yields a stable equilibrium point if the second derivative of U is > 0 and an unstable equilibrium point if it is < 0 .

4.2 Analysis of a Three-Spring Stack

The three-spring stack model is given in Figure 9. Like the previous formulation, each spring can have a different height, labeled as h_1 , h_2 , and h_3 . Now, two simultaneous equations equating the forces in each spring can be written as:

$$\frac{M}{2}(\delta_{st} - \delta_2)^3 - \frac{3h_3M}{2}(\delta_{st} - \delta_2)^2 + (h_3^2M + N)(\delta_{st} - \delta_2) = \frac{M}{2}(\delta_2 - \delta_1)^3 - \frac{3h_2M}{2}(\delta_2 - \delta_1)^2 + (h_2^2M + N)(\delta_2 - \delta_1) \quad (11)$$

$$\frac{M}{2}(\delta_2 - \delta_1)^3 - \frac{3h_2M}{2}(\delta_2 - \delta_1)^2 + (h_2^2M + N)(\delta_2 - \delta_1) = \frac{M}{2}(\delta_1)^3 - \frac{3h_1M}{2}(\delta_1)^2 + (h_1^2M + N)(\delta_1) \quad (12)$$

Then, the force in the stack associated with each $\{\delta_1, \delta_2\}$ solution set can be found from:

$$F = \gamma \left[\frac{M}{2}(\delta_{st} - \delta_2)^3 - \frac{3h_3M}{2}(\delta_{st} - \delta_2)^2 + (h_3^2M + N)(\delta_{st} - \delta_2) \right] \quad (13)$$

The potential energy U of the three-spring stack is given by:

$$U = \gamma \left[\left(\frac{M}{8}(\delta_{st} - \delta_2)^4 - \frac{h_3M}{2}(\delta_{st} - \delta_2)^3 + \frac{h_3^2M+N}{2}(\delta_{st} - \delta_2)^2 \right) + \left(\frac{M}{8}(\delta_2 - \delta_1)^4 - \frac{h_2M}{2}(\delta_2 - \delta_1)^3 + \frac{h_2^2M+N}{2}(\delta_2 - \delta_1)^2 \right) + \left(\frac{M}{8}\delta_1^4 - \frac{h_1M}{2}\delta_1^3 + \frac{h_1^2M+N}{2}\delta_1^2 \right) \right] \quad (14)$$

The stability of each equilibrium point $\{\delta_1, \delta_2\}$ is evaluated using the Hessian matrix, H , given by:

$$H = \begin{bmatrix} \frac{\partial^2 U}{\partial \delta_1^2} & \frac{\partial^2 U}{\partial \delta_1 \partial \delta_2} \\ \frac{\partial^2 U}{\partial \delta_2 \partial \delta_1} & \frac{\partial^2 U}{\partial \delta_2^2} \end{bmatrix} \quad (15)$$

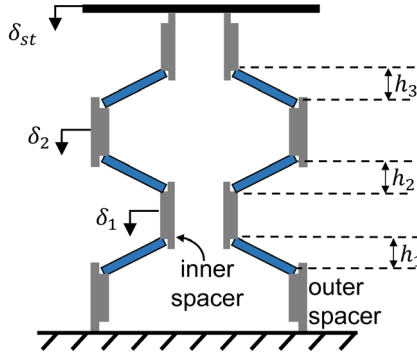


Figure 9: Model of three-spring stack where each spring can have different height and therefore different h/τ ratio. The input is δ_{st} and δ_1 and δ_2 are displacement (response) coordinates.

The equilibrium point is a local minimum if both eigenvalues of H are positive, a local maximum if both eigenvalues of H are negative, and a saddle point if one eigenvalue is positive and one is negative. The equilibrium point is stable only if both eigenvalues are positive.

4.3 Analysis of Stacks with an Arbitrary Number of Springs

The system can be now generalized for an arbitrary number of springs as in Figure 10. For a displacement-controlled stack with n springs, there are $n - 1$ displacement variables $\{\delta_1, \delta_2, \dots, \delta_{n-1}\}$. Then using Eqn. (1), the forces in each disk spring can be related by:

$$\begin{aligned} P(\delta_{st} - \delta_{n-1}) &= P(\delta_{n-1} - \delta_{n-2}) \\ P(\delta_{n-1} - \delta_{n-2}) &= P(\delta_{n-2} - \delta_{n-3}) \\ &\vdots \\ P(\delta_2 - \delta_1) &= P(\delta_1) \end{aligned} \tag{16}$$

The above $n - 1$ nonlinear algebraic equations are numerically solved at each value of δ_{st} to find the displacements $\{\delta_1, \delta_2, \dots, \delta_{n-1}\}$. Then, the force for each set of solutions can be found from:

$$F = P(\delta_{st} - \delta_{n-1}) \tag{17}$$

The Hessian matrix is used as before to classify the stability of each fixed point:

$$H = \begin{bmatrix} \frac{\partial^2 U}{\partial \delta_1^2} & \cdots & \frac{\partial^2 U}{\partial \delta_1 \partial \delta_n} \\ \vdots & \ddots & \vdots \\ \frac{\partial^2 U}{\partial \delta_n \partial \delta_1} & \cdots & \frac{\partial^2 U}{\partial \delta_n^2} \end{bmatrix} \tag{18}$$

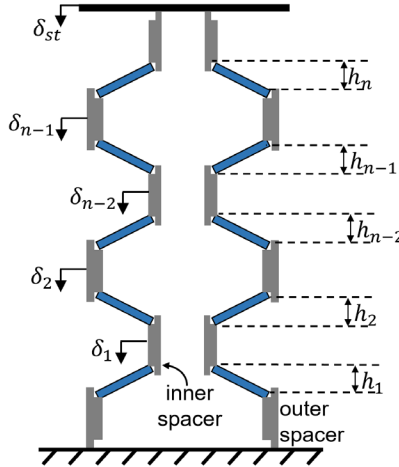


Figure 10: Stack with an arbitrary number of springs and displacement coordinates where each spring can have a different height, and δ_{st} is the input.

As the number of springs increases, the order of the system goes up and the potential energy landscape becomes more complex. However, the same general procedures can be used to determine the force-deflection, stiffness, and other nonlinear characteristics including snap-through and directional dependence, as illustrated in the next section.

5. Nonlinear Force-Deflection Characteristics and Stability Maps

5.1 Effect of Variations on the Two-Spring Stack Properties

It is not feasible to individually evaluate every h/τ ratio combination of springs in a stack. Instead, we focus on eight specific cases that are illustrative of the nonlinear behavior that can occur in large sets of h/τ combinations. These cases are defined in Table 3. We first consider Cases 1-3. Case 1 has two springs with h/τ ratio < 1.41 , Case 2 has one spring with h/τ ratio < 1.41 and one spring with h/τ ratio > 1.41 , and Case 3 has two springs with h/τ ratio > 1.41 . The force-deflection and stiffness-deflection for the individual springs found in Cases 1-3 are plotted in Figure 11 according to Eqns. 1 and 2. The highly nonlinear characteristics are evident by the stiffness changing by several hundred N/mm in less than 0.5 mm deflection. As expected, the springs with h/τ ratio > 1.41 have negative stiffness at the deflection midpoint ($\delta = h$). The stiffnesses of each spring at the midpoint are 19.1, 11.4, -35.5, and -50 N/mm for $h/\tau = 1.32, 1.36, 1.58$, and 1.64 respectively.

Table 3: The h/τ ratios for Cases 1-5 of a two and three-spring stacks considered in this paper. Cases 1-5, and 8 are for two-spring stacks. Cases 6-7 are for three-spring stacks.

	Case 1	Case 2	Case 3	Case 4	Case 5	Case 6	Case 7	Case 8
$\frac{h_1}{\tau}$	1.32	1.36	1.58	1.6	1.9	1.32	1.54	1.69
$\frac{h_2}{\tau}$	1.36	1.58	1.64	2.1	1.95	1.36	1.58	1.75
$\frac{h_3}{\tau}$						1.58	1.62	

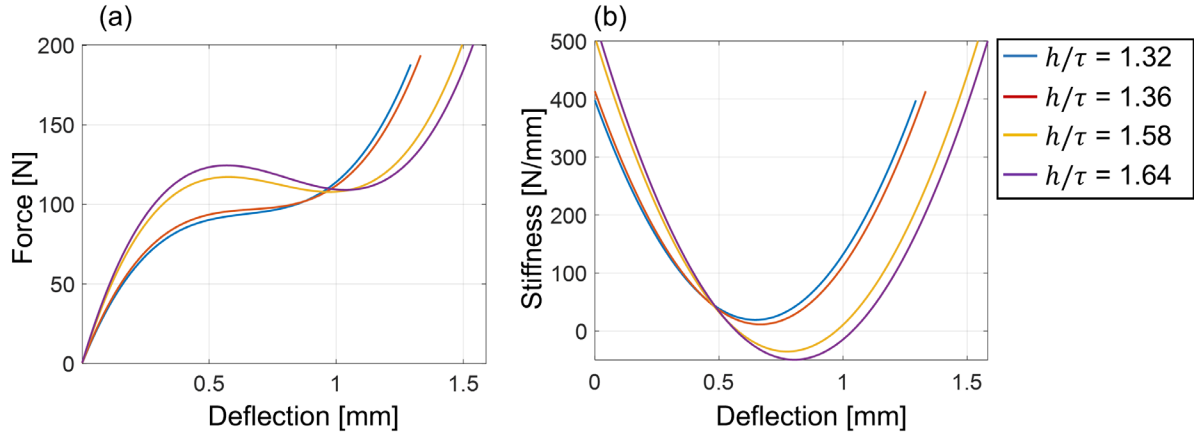


Figure 11: Force-deflection (a) and stiffness-deflection (b) curves of single coned disk springs with h/τ ratios for Cases 1 and 2 of Table 3.

Next, calculated force-deflection solutions of the stacks (Case 1, Case 2, and Case 3) are shown in Figure 12. It is observed that important nonlinear characteristics including multiple stability regimes occur within the QZS region; this is where we focus our analysis. Stable equilibrium points are shown as filled circles while unstable points are shown as unfilled circles. For Case 1, only one solution exists for all δ_{st} values. Case 2 also has only one equilibrium at every point, but significant nonlinearity is observed in the QZS region. Case 3 has two negative stiffness regions associated the successive buckling of each spring and a region between 1.3 and 2 mm where 3 equilibrium points exist (two stable equilibria and one unstable equilibrium).

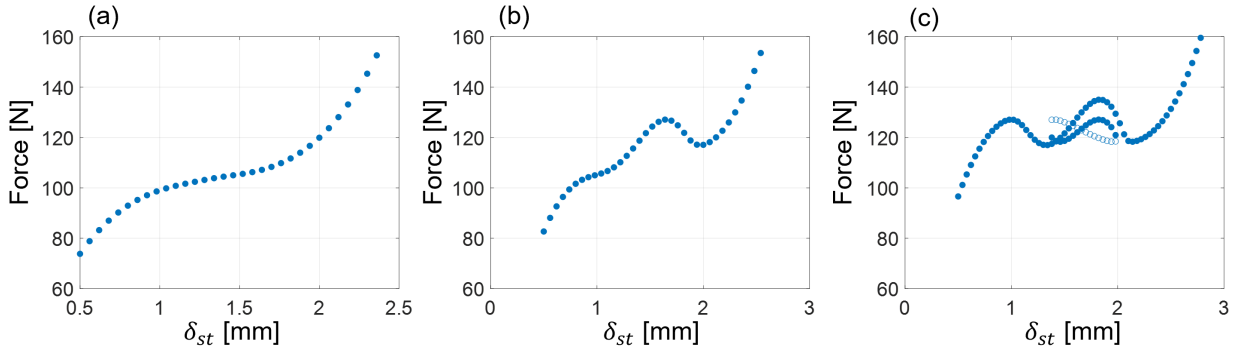


Figure 12: Calculated force-deflection curves of stacks for Case 1 (a), Case 2 (b), and Case 3 (c), corresponding to the elements of Table 3 and Fig 11. Here, a filled circle indicates a stable equilibrium point and an unfilled circle indicates an unstable equilibrium point.

To get a broader perspective of when multiple equilibrium points exist, we use Eqn. 8 to determine the multi-regimed stability conditions for a wide range of h/τ values. In Figure 13, the h_1/τ ratio of spring 1 is on the x-axis and the h_2/τ ratio of spring 2 is on the y-axis. The dark area indicates where three equilibrium points exist, and the lighter area indicates where only one equilibrium point exists. The graph is symmetric with respect to the diagonal, indicating that the arrangement of the springs in the stack does not affect the stability. It is observed that multiple equilibria can exist even when one of the springs has h/τ ratio less than 1.41. For example, multi-stability exists when spring 1 has $h_1/\tau = 1.35$ and spring 2 has $h_2/\tau = 2.1$. Another interesting characteristic is that multi-regimed stability can occur at lower h/τ ratios the closer h_1/τ and h_2/τ are to each other. For example, such regimes occurs when $h_1/\tau = 1.45$ and $h_2/\tau = 1.46$, but does not occur when $h_1/\tau = 1.45$ and $h_2/\tau = 1.55$.

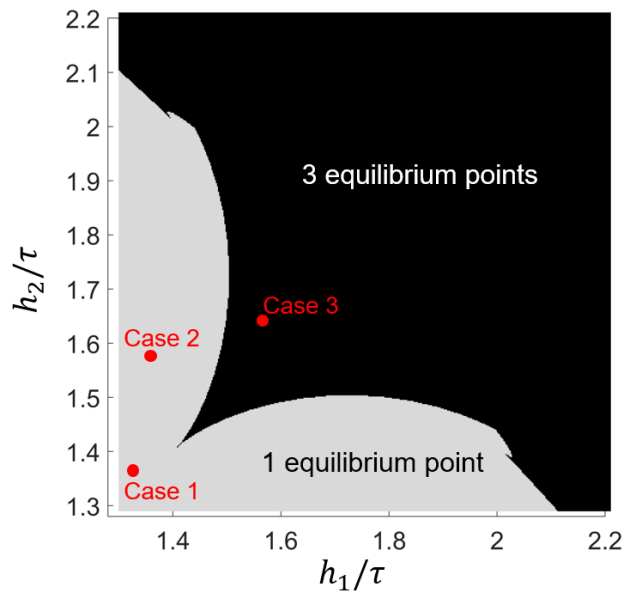


Figure 13: Multi-regimed stability regimes as a function of h_1/τ and h_2/τ for a two-spring stack for Cases 1, 2 and 3.

In the two-spring stack, multi-stability refers to the displacement coordinate δ_1 having multiple possible values for a given input δ_{st} . To illustrate this point, we consider the potential energy, U , as a function of δ_1 for Case 3. As shown in Figure 14a, two new equilibrium points (one potential energy minimum and one potential energy maximum) are created when δ_{st} reaches approximately 1.4 mm, which can also be seen from Figure 12c. When δ_{st} increasing beyond 2.0 mm, those two equilibrium points vanish, and a single equilibrium point remains for larger δ_{st} . If the displacement starts from zero or the maximum value ($\delta_{st} = 2.8$ mm), the system remains in the same potential well over the entire stroke, as indicated by the dashed red lines in Figure 14a. Therefore, the additional stable equilibrium point created in the QZS regime is not accessed unless a perturbation is made to δ_1 which forces the system out of this potential well. This behavior can also be understood by considering the displacement δ_1 as a function of δ_{st} in Figure 14b. The coordinate δ_1 remains along the same stable trajectory starting from either $\delta_{st} = 0$ or $\delta_{st} = 2.8$. The additionally equilibrium points exist at lower δ_1 values and are not accessed. As a result, the force-deflection curve should not have any direction dependence without a perturbation to δ_1 .

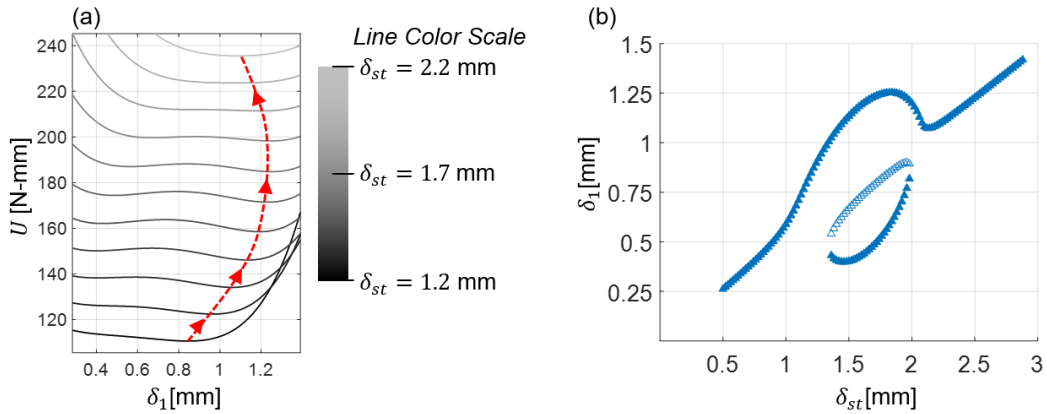


Figure 14: Potential energy U of Case 3 as a function of δ_1 for a range of δ_{st} values (a), and δ_1 solutions as a function of δ_{st} (b). Here, an unfilled circle in (b) indicates an unstable equilibrium point.

5.2 Snap-Through Events for Two-Spring Stack Given Variations

Another important nonlinear behavior in two-spring stacks is the occurrence of snap-through events. In Case 3, there are successive regions of negative stiffness in the QZS region, but these are not snap-through events because δ_1 remains along a stable trajectory throughout the stroke. A snap-through event occurs if the potential well in which the system resides is eliminated upon a small change in δ_{st} , and there is a jump to a new potential well. Under these circumstances, the force-deflection curve can have a direction dependence (loading versus unloading). Force-deflection curves of many two spring stacks are simulated to determine the h/τ ratios which result in snap-through events. In the two-spring stack, δ_{st} is the controlled input and snap-through events are associated with a jump in δ_1 and F . Figure 15a shows a map that indicates where snap-through events occur as a function of the h/τ ratios (h_1/τ on the x-axis and h_2/τ on the y-axis). There is a distinct boundary between regions of snap-through and no snap-through. The boundary is defined by a straight line with fitted equation of $h_2/\tau =$

$-h_1/\tau + 3.35$. Similar to the existence of multiple equilibrium points, snap-through can exist even when one of the springs has h/τ less than 1.41 if the other h/τ ratio is high enough.

Figure 15a is a binary map showing if snap-through exists, but it doesn't say anything about the strength of the snap-through. One measure of the strength is the change in force that occurs during the snap-through event. A contour map in Figure 15b shows the snap-through force as a function of h_1/τ and h_2/τ . Similar to existence of multiple equilibrium in Figure 13, the snap-through strength depends on the closeness of the two h/τ ratios. When they are far apart (for example when $h_1/\tau = 1.5$ and $h_2/\tau = 2.1$), the snap-through force is large (-45 N jump). As the ratios become closer, the snap-through force becomes smaller.

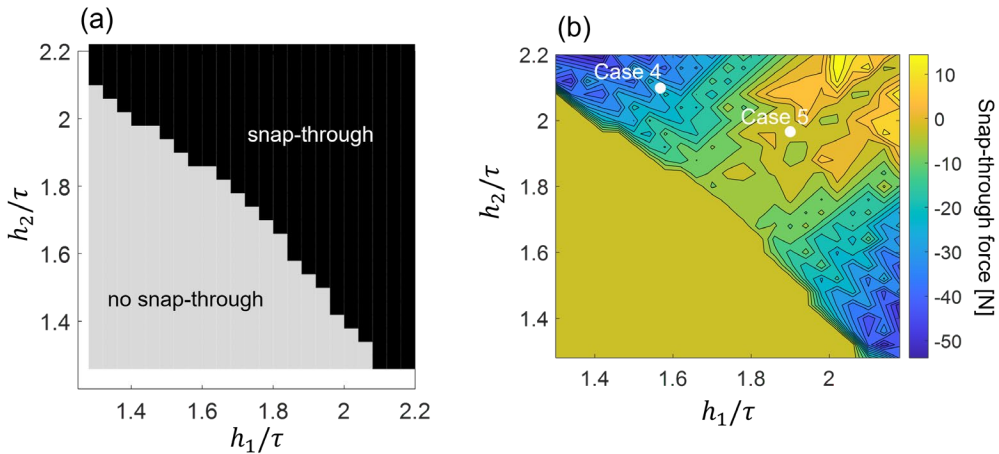


Figure 15: Snap-through event maps in a two-spring stack as a function of h_1/τ and h_2/τ (a), and similar map indicating the strength of the snap-through event as measured by the snap-through force (b).

Snap-through behavior is considered in more detail by examining some specific cases. Case 1, Case 2, and Case 3 lie in the no snap-through region, and Figure 12 confirms that there are no snap-through events for these cases. The locations of Case 4 and Case 5 on the snap-through map are indicated in Figure 15b. The force as a function of δ_{st} and δ_1 as a function of δ_{st} are given for Case 4 in Figure 16a-b and for Case 5 in Figure 16c-d. For Case 4, as δ_{st} starts from 0 mm and monotonically increases, a snap-through takes place at approximately $\delta_{st} = 2.45$ mm which involves a jump in both the force (Figure 16a) and δ_1 (Figure 16b). The snap-through is associated with destruction of one stable and one unstable equilibrium point, and the system jumps to the only remaining potential well. During unloading, the system stays in this potential well until $\delta_{st} = 1.7$ mm, creating a direction-dependent force-deflection curve and hysteresis. Case 5 has some similar characteristics, but the snap-through at $\delta_{st} = 2.7$ mm during loading and at $\delta_{st} = 1.2$ mm during unloading have much smaller forces compared to those for Case 4. Here, δ_1 takes a substantially different path between loading and unloading, but the force-deflection curve does not have significant direction dependence. This physically makes sense because as the springs become closer to being identical, the two stable equilibrium paths should have the same force due to the symmetry of this system.

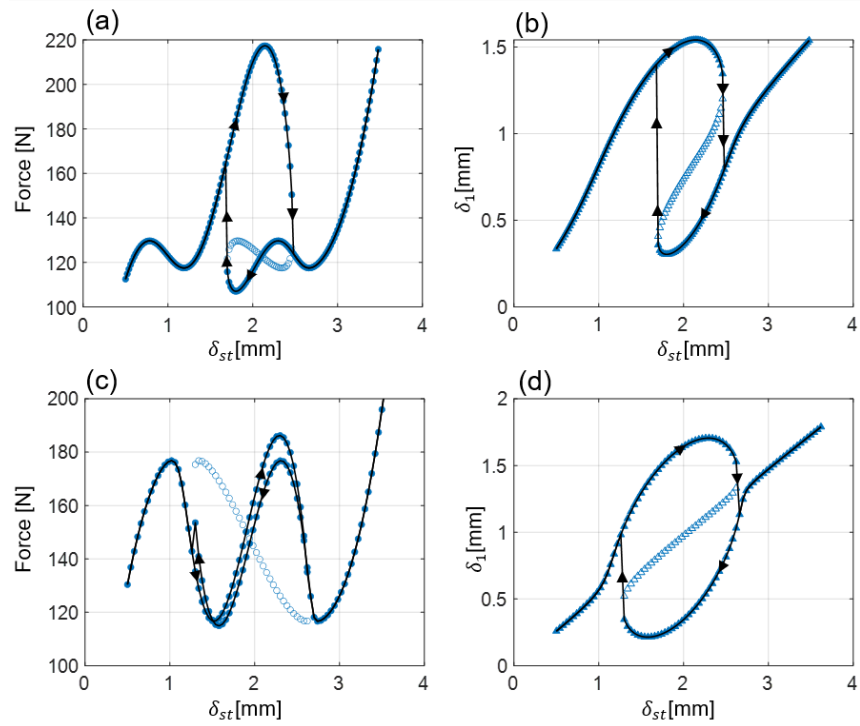


Figure 16: Multi-regimed mapping for Cases 4 and 5 of Table 3. Force versus δ_{st} for Case 4 (a), δ_1 versus δ_{st} for Case 4 (b), force versus δ_{st} for Case 5 (c), δ_1 versus δ_{st} for Case 5 (d).

5.3 Three-Spring Stack Properties Given Variations

As the number of springs in the stack increases, the number of response (displacement) coordinates increases, and the potential energy landscape can become increasingly more complex. While a comprehensive analysis of stacks with more than two springs is beyond the scope of this article, Cases 6 and 7 are considered to illustrate the implications.

The force versus δ_{st} for Case 6 is plotted in Figure 17a. Equilibrium points are identified as stable, unstable, or saddle points by black circles, white circles, and gray circles respectively. The force characteristics are similar to Case 2, and there is only one stable equilibrium point for every value of δ_{st} . On the other hand, new characteristics are observed in Case 7 load-deflection plotted in Figure 17b. First, stable points, unstable points, and saddle points are all seen in the plot. Second, a snap-through event occurs at $\delta_{st} = 3.1$ mm and is associated with the destruction of a saddle point and stable point. This snap-through occurs at much lower h/τ ratios than would result in snap-through in a two-spring stack. Therefore, one important consequence of increasing the number of springs is that snap-through can occur even at smaller h/τ ratios.

Another important consequence is that the engineered system becomes significantly more complex, and up to seven equilibria are found for certain values of δ_{st} . These equilibria are defined by different sets of $\{\delta_1, \delta_2\}$. As an example, the potential energy map at $\delta_{st} = 2.7$ mm is plotted as a function of δ_1 and δ_2 in Figure 18. Out of the seven equilibrium points, three are stable, one is unstable, and three are saddle points. The equilibrium points have widely varying

values of δ_1 and δ_2 , but the force does not have such a wide variation, ranging only from 118 to 125 N. Furthermore, the potential energy of the equilibrium points varies by even less. The minimum potential energy is 269 N-mm, which occurs at the stable equilibrium point in the upper right corner, and the maximum is 275 N-mm, which occurs at the unstable equilibrium point. While such multi-regimed stability may be an additional challenge created by the disk-to-disk variation for QZS isolation, this simple stack can be designed to have a wide range of multi-stability conditions. Therefore, it may have interesting advantages where multi-regimed stability is desired such as for wave energy absorption, structural computing, or sensing [35].

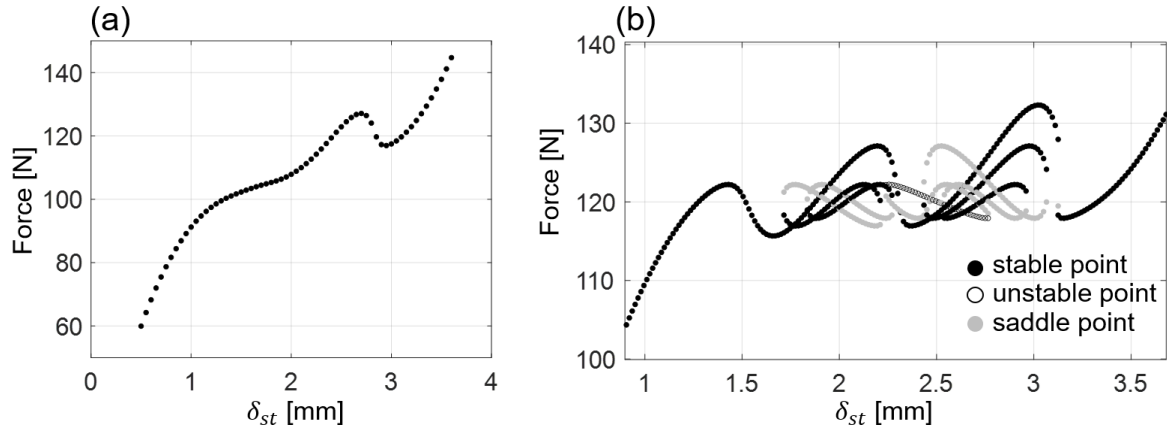


Figure 17: Stability maps for 3-Spring Stacks. Force-deflection for Case 6 (a) and Case 7 (b) showing stable points, unstable points, and saddle points.

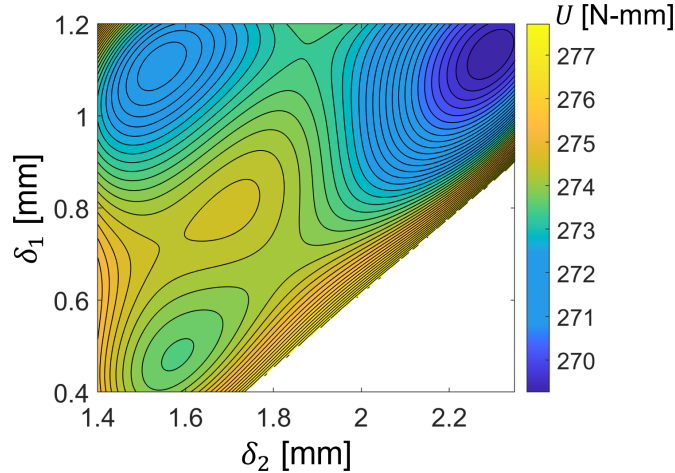


Figure 18: Potential energy map of Case 7 (3-prong stack) at $\delta_{st} = 2.7\text{mm}$

6. Nonlinear Stiffness Characteristics and QZS Isolator Considerations

In addition to the nonlinear force-deflection characteristics, the stack stiffness is also a crucial consideration with respect to the design of QZS isolators. An important question becomes how to account for the disk-to-disk variability in the stiffness design. One approach is to try to avoid it by reducing the disk-to-disk variation. If the goal is to design an isolator with

smooth and flat QZS region as is typically done, springs with $h/\tau > 1.41$ should be avoided because it leads to both successive regions of negative stiffness and widely varying stiffness in the QZS region. The stiffness versus stack displacement for Cases 1, 2, and 3 are shown in Figure 19a. The stiffness of Case 1 reaches a minimum of 9.1 N/mm at 1.45 mm deflection, which is smaller magnitude than the stiffness of either spring used to construct it (19.1 and 11.4 N/mm). This is the same behavior as that of linear springs in series. The other two cases each have multiple local minima associated with the successive buckling of each spring. Case 2 has a local minimum of 18 N/mm at 0.9 mm displacement, but another minimum at 1.78 mm which is negative (-51 N/mm). Not only is this stiffness negative, but it has a larger maximum negative stiffness than either of the spring stiffnesses used to construct it (11.4 N/mm and -35.5 N/mm). Similarly, Case 3 has a local minimum of -109 N/mm at 2 mm, which is a significantly larger magnitude than the maximum negative stiffness of either of its individual springs.

Calculated stiffnesses of the three-spring stacks (Cases 6 and 7) are displayed in Figure 19b. Case 6 has a similar trend to Case 2. Both Case 2 and Case 6 have springs with h/τ ratio below 1.41 and one spring with h/τ ratio of 1.58. However, the maximum negative stiffness of Case 6 is much larger than Case 2. It is observed from Cases 2, 3, 6, and 7 that instead of the magnitude of negative stiffness being attenuated upon stacking, the negative stiffness becomes amplified as the number of springs is increased, even if only one of the springs has $h/\tau > 1.41$. This presents a significant challenge with respect to the design of QZS isolators, which are intended to have close to zero stiffness in the QZS region. The stack achieves a smaller minimum stiffness compared to that of its individual springs only when all of the springs in the stack have $h/\tau < 1.41$. Additionally, the stiffness becomes more linear and constant over a much larger displacement, which is the original intent of stacking. Therefore, if the variation can be somehow controlled, but not eliminated, it may be desirable to keep the variations under $h/\tau = 1.41$.

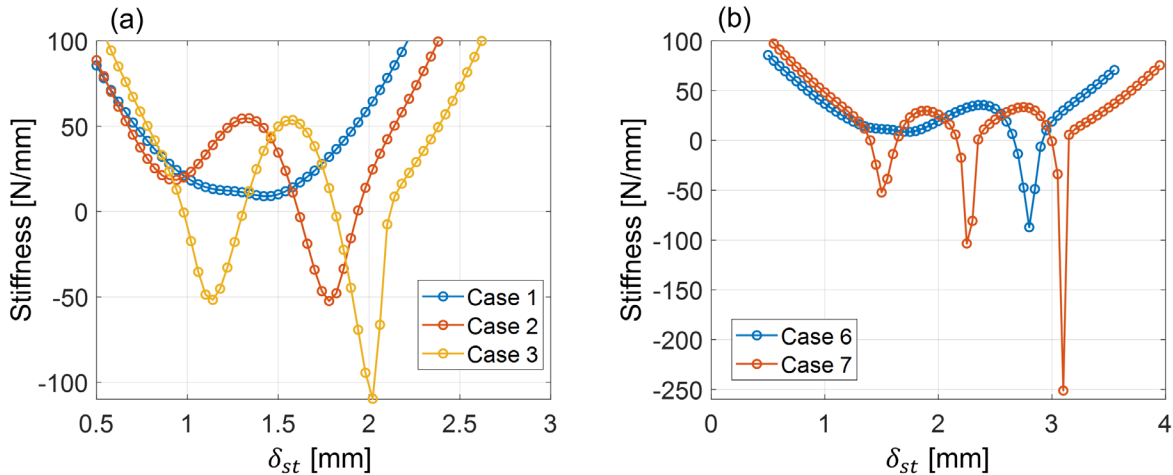


Figure 19: Stack stiffness as a function of the input displacement for Cases 1-3 (a), and Cases 6-7 (b).

Even if the maximum h/τ can be kept below 1.41, there is no simple formula (or a design guideline) which can predict the minimum stiffness in the QZS region for disk spring stacks with

non-identical springs. The system of equations must be solved for each distinct combination of springs. We solve the system for a range of h_1/τ and h_2/τ less than 1.41 and determine a trend for how the minimum stack stiffness varies. Figure 20a shows the minimum stack stiffness of a two-spring stack as a function of the minimum stiffness of each spring on the y and x axes respectively. Equivalent stiffness of two linear springs in series is shown in Figure 20b. The dashed diagonal lines are the lines along which the springs are identical. At points near the diagonal line in Figure 20a, the minimum stack stiffness approaches half the minimum stiffness of the individual springs. This makes sense because if the springs are identical, they will always have the same deflection and therefore the stiffness is simply scaled linearly from the stiffness of individual single springs. Along this diagonal line, the minimum stiffness is the same as the equivalent stiffness two linear springs in series.

This is the best-case scenario because away from the diagonal line of Figure 20a, the minimum stiffness is always higher than the equivalent stiffness of a linear spring stack. For example, when spring 1 minimum stiffness is 20 N/mm, and spring 2 minimum stiffness is 20 N/mm, the minimum stack stiffness is 10 N/mm. The equivalent stiffness of two linear springs each with stiffness of 20 N/mm is also 10 N/mm. However, if spring 1 minimum stiffness remains 20 N/mm but spring 2 minimum stiffness becomes 40 N/mm, the minimum stack stiffness increases to 16 N/mm. The equivalent stiffness of two linear springs with stiffnesses of 20 and 40 N/mm is 13.3 N/mm. Therefore, there it is again desirable to keep the h/τ ratios not only less than 1.41, but to keep the h/τ variation as small as possible to minimize the overall minimum stiffness.

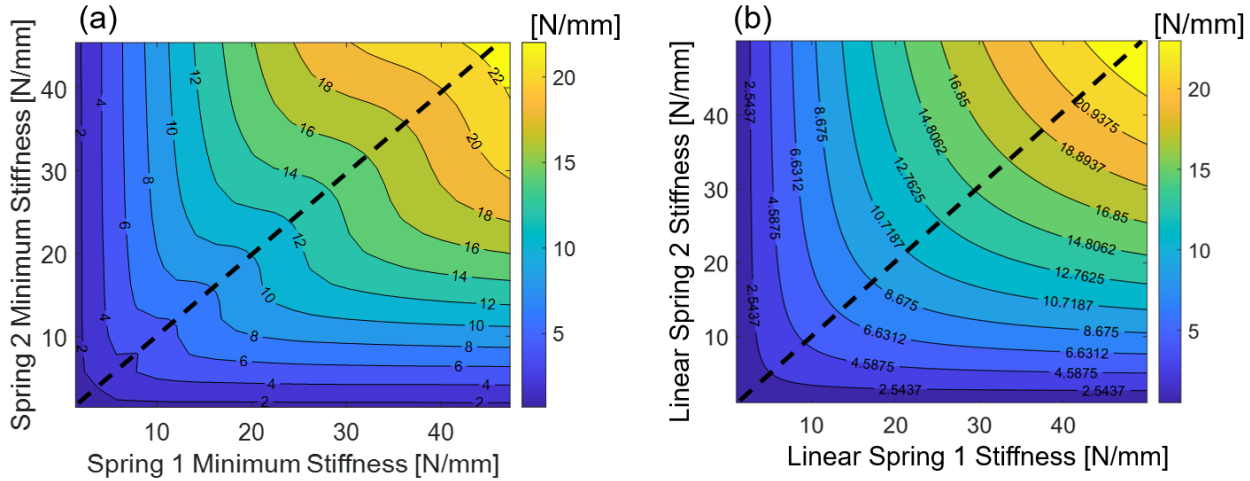


Figure 20: Minimum stiffness in QZS region as a function of the minimum stiffnesses of Spring 1 and Spring 2 in a two-spring stack (a), and equivalent stiffness of two linear springs in series (b).

If the variation cannot be meaningfully reduced (likely in a manufacturing setting), a second approach is to try to exploit the highly nonlinear behavior in the QZS region. For example, the hysteresis in the QZS region created by snap-through events may contribute some structural damping that could be advantageous in the vibration attenuation, say at resonances. Furthermore, directional dependence exists only if δ_{st} goes beyond certain values, and therefore hysteretic damping could be achieved (without adding any damping) when specific vibration

amplitudes are exceeded. Nonetheless, this strategy may be difficult to implement because the stack force-deflection curve with a random set of springs would still be somewhat unpredictable as demonstrated in Figure 7.

A third possible approach to manage the disk-to-disk variation is such a way that compares the QZS working range of individual springs to the expected vibration amplitudes. In particular, if the deflections of individual springs are designed to be very small compared to the expected vibration amplitude, the overall effective dynamic stiffness may still be close to zero. But this approach requires the number of springs in the stack to be large. To illustrate this example, we constructed a disk-spring stack made from a different commercial spring with very small height (~0.4 mm). The stack contains 16 individual springs in series and its measured force-deflection curve is plotted in Figure 21. The curve has many successive snap-through events, but their amplitudes and deflections are smaller when compared to the overall force and deflection of the stack as a whole. If the vibration amplitude is 3 mm, for example, the effective dynamic stiffness therefore may still be close to zero. This approach has its own set of challenges, but it poses an interesting design option depending on the application scenario.

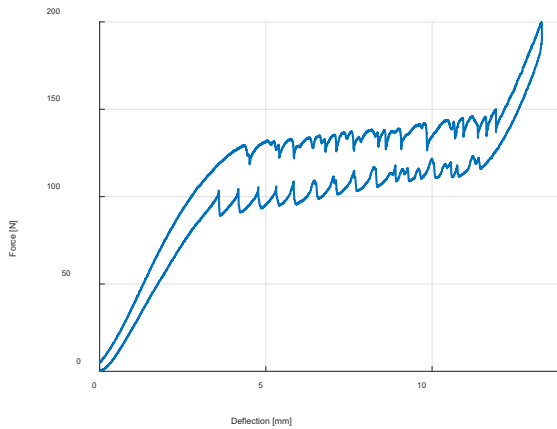


Figure 21: Measured properties of an engineered stack made from 16 individual disk springs each with a nominal height of 0.4 mm.

7. Experimental Validation

7.1 Nonlinear Static Behavior

Experimental validation of nonlinear static behavior is done using Case 8 of Table 3. Two disk springs with h/τ ratio > 1.41 were randomly selected for the stack design. Their heights of 0.84 and 0.875 mm are measured using a laser microscope, and the resulting h/τ ratios are 1.69 and 1.75 respectively. Equations 5-6 are used to simulate a stack with these springs. Figure 22 compares the measured and computed force-deflection curves. First, the experimental data shows no direction-dependent force-deflection behavior other than hysteresis due to edge friction. This is expected based on where Case 8 falls on the snap-through map of Figure 15. Overall, the model predicts higher forces in the QZS region, but the overall trend and behavior are similar to the experiment. Higher predicted forces from the model may be due to

the loads not being perfectly distributed around the circumference in the experiment (due to slight misalignments and assembly errors).

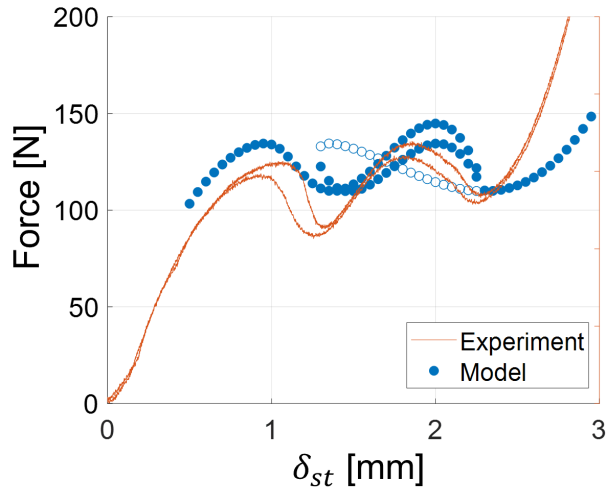


Figure 22: Experimental validation of Case 8 force-deflection results (model showing both stable (filled circles) and unstable (unfilled circles) solutions).

Next, we aim to demonstrate the multi-regimed stability characteristic as both Figure 13 and Figure 22 show this behavior is expected in Stack 8. The experimental force-deflection setup is modified with a second laser sensor to measure the displacement δ_1 . As seen in Figure 23, a plastic tab is attached to the outer spacer and serves as a measurement surface for laser sensor 2. Using this setup, δ_{st} , δ_1 , and F can be measured simultaneously for comparison to theoretical results. The experimental procedure outlined in Figure 24a is used to get the stack in both stable positions during the loading phase. First, the stack is displaced to the region where two stable solutions should exist. It is known based on the geometry and stack force-deflection results that the system will remain along the same stable trajectory from unloaded to fully compressed. Therefore, a perturbation to δ_1 is needed to access the second stable position in the range of $1.3 < \delta_{st} < 2.3$ mm. Once the stack is loaded to $\delta_{st} < 1.5$ mm, the middle spacer is pushed down access the second stable position. This process can be seen graphically in Figure 24b which shows δ_1 as a function of δ_{st} (for both the experiment and the model). The experiment shows the existence of a second stable position of δ_1 . Once δ_{st} goes beyond 2 mm, the second stable equilibrium is destroyed, and δ_1 jumps back to the original trajectory. Then upon unloading, δ_1 remains along the original trajectory without accessing the second stable position. Therefore, both this experiment and the overall force-deflection behavior show the same nonlinear characteristics that are expected from the model.

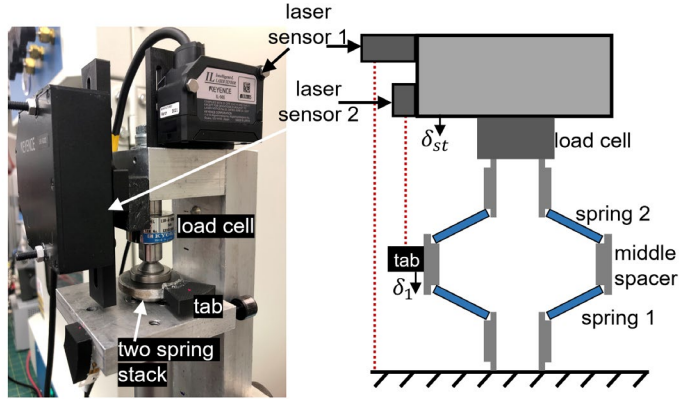


Figure 23: Modification of the force-deflection setup with a second laser sensor to measure response δ_1 . The setup measures force, input δ_{st} , and response δ_1 simultaneously as the stack is loaded and unloaded.

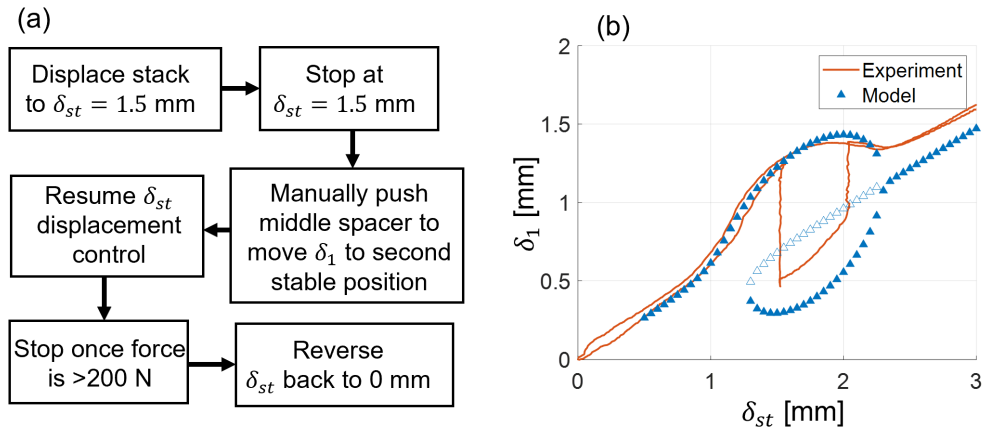


Figure 24: Experimental procedure for demonstrating and measuring multi-regimed stability in Case 8 (a). and response δ_1 as a function of input δ_{st} during execution of the procedure in (a). Here, filled triangles are stable and unfilled triangles are unstable points.

7.2 Vibration Isolation Experiment

Experimental validation of the vibration isolation with disk spring stacks is accomplished by the base displacement excitation experiment as pictured in Figure 25a. Both Stack A and Stack B of Figure 7 are evaluated. Each stack is placed between an electrodynamic shaker and a 10.7 kg mass, which puts the static equilibrium position in the QZS region of each stack. Guide shafts constrain the motion of the mass to the vertical direction. Constant displacement amplitude sine sweeps at 8 Hz/min sweep rate are generated using VibrationView closed loop controller from Vibration Research. Accelerometers are attached to the shaker and top of the mass, and the signals are recorded with VibrationView software.

The transmissibility spectra are plotted in Figure 25b for each stack subject to two (0.75 and 1.0 mm) amplitudes. Stack A achieves isolation after 6.8 Hz for both input amplitudes while Stack B achieves isolation after approximately 7.5 Hz. Stack A also has lower transmissibility in the lower frequency region between 3 and 6 Hz. Important observations of the measurements are as follows. First, the disk spring stack is demonstrated to be compact and effective vibration

isolator. Second, the disk-to-disk variation is seen to affect the vibration isolation performance and therefore this issue becomes an important design consideration. Third, the dynamic response results combined with the static characteristics show that there are many possibilities for further improving the isolation performance of disk spring stacks. Therefore, we anticipate that disk spring stacks have good potential as practical QZS structures if the disk-to-disk variations can be effectively managed.

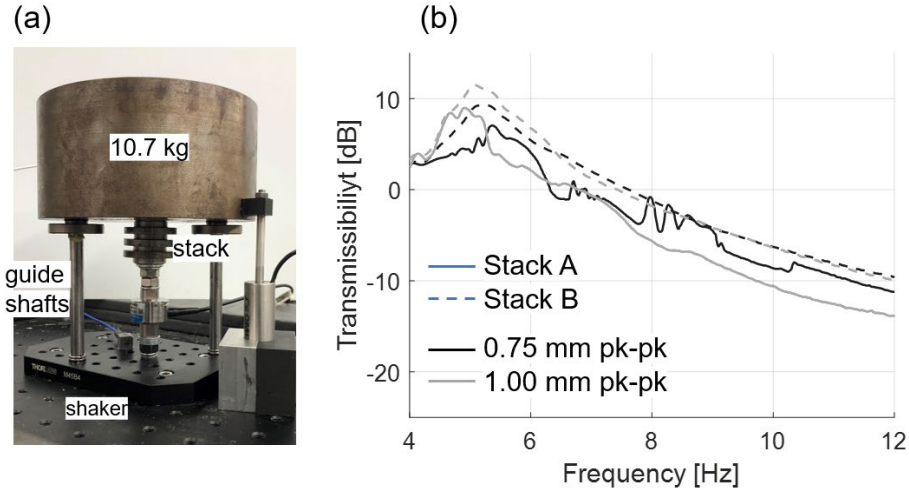


Figure 25: Dynamic responses of disk spring stacks with a rigid mass forming a single-degree-of freedom system: experimental setup with electrodynamic shaker providing base excitation in the vertical direction only (a), and transmissibility spectra for Stack A and Stack B at two different excitation amplitudes (b).

8. Conclusion

This article introduces a novel approach to designing an isolator stack that integrates commercially available disk springs with particular geometries to achieve the desired nonlinear force deflection behavior within a quasi-zero stiffness (QZS) domain. It leverages the inherent static responses of stacked disks, as discussed herein, enabling the creation of low-cost, compact vibration isolators. A significant hurdle when utilizing commercial disk springs is the variability between disks, a result of manufacturing tolerances. This aspect of variability has been overlooked by previous researchers, who have operated under the assumption that all disks in a stack are identical. To address this, we analyzed one hundred disk springs to gauge their variability and how factors like elastic modulus, edge friction, and geometry influence overall stack performance. Our findings indicate that manufacturing tolerances substantially affect the stack's nonlinear force-deflection profile. A computational method to consider these individual disk spring variations has been presented in assessing the stack's functionality. This has been corroborated through experimental studies for both static and dynamic properties.

While multi-regimed stability issues pose an additional challenge created by the disk-to-disk variation for QZS isolation, disk stacks could be designed to have a wide range of multi-stability conditions to meet interesting wave energy absorption, structural computing, or sensing needs [35]. Overall, this article not only lays the groundwork for further advancements in disk spring-based QZS isolators but also highlights potential areas for product enhancement, such as in damping optimization and reducing height variance. Moreover, the experimental investigations presented in this paper are poised to inspire future work aimed at refining force-deflection relationships across various stiffness regimes.

References

- [1] J.O. Almen, A. Laszlo, The uniform-section disk spring, *Trans. ASME* 58 (1936) 305–313.
- [2] G. Curti, M. Orlando, A new calculation of coned annular disk spring, *Proceedings of the ASME Winter Annual Meeting*, New York, (1976) 76-WA / DE-9.
- [3] G. Curti, R. Montanini, On the influence of friction in the calculation of conical disk springs, *Transactions of the ASME* (1999) 121 622–627.
- [4] S. Ozaki, K. Tsuda, J. Tominaga, Analyses of static and dynamic behavior of coned disk springs: effects of friction boundaries, *Thin-Walled Structures* 59 (2012) 132–143.
- [5] N. P. Mastrolia, J. T. Dreyer, R. Singh, Analytical and experimental characterization of nonlinear coned disk springs with focus on edge friction contribution to force-deflection hysteresis, *Mechanical Systems and Signal Processing* 91 (2017) 215-232.
- [6] P. Bühl, Mechanische Schwingungen bei Tellerfedersäulen, *DRAHT –Fachzeitschrift* (2) (1977) 48–53.
- [7] American National Standards Institute, Mechanical Vibration and Shock—Evaluation of Human Exposure to Whole Body Vibration—Part 4: Guidelines for the Evaluation of the Effects of Vibration and Rotational Motion on Passenger and Crew Comfort in Fixed-Guideway Transport Systems (ANSI S2.72-2003) (2007).
- [8] I. Kovacic, M.J. Brennan, T.P. Waters, A study of a nonlinear vibration isolator with a quasi-zero stiffness characteristic, *Journal of Sound and Vibration* 315.3 (2008) 700-711.
- [9] C. Liu, W. Zhang, K. Yu, T. Liu, Y. Zheng, Quasi-zero-stiffness vibration isolation: Designs, improvements and applications, *Engineering Structures* 301, (2024) 117282.
- [10] A. Carrella, M.J. Brennan, T.P. Waters, Static analysis of a passive vibration isolator with quasi-zero-stiffness characteristic, *Journal of Sound and Vibration* 301.3-5 (2007) 678-689.
- [11] J. Zhou, X. Wang, Y. Mei, Characteristic analysis of a quasi-zero-stiffness vibration isolator, *IOP Conference Series: Materials Science and Engineering* 397.1 (Aug. 2018) 012045.
- [12] S. Wang, W. Xin, Y. Ning, B. Li, Y. Hu, Design, experiment, and improvement of a quasi-zero-stiffness vibration isolation system, *Applied Sciences* 10.7 (2020) 2273.
- [13] Y. Jiang, C. Song, C. Ding, B. Xu, Design of magnetic-air hybrid quasi-zero stiffness vibration isolation system, *Journal of Sound and Vibration* 477 (2020) 115346.
- [14] X. Sun, X. Jing, Analysis and design of a nonlinear stiffness and damping system with a scissor-like structure, *Mechanical Systems and Signal Processing* 66 (2016) 723-742.
- [15] X. Jing, Y. Chai, X. Chao, J. Bian, In-situ adjustable nonlinear passive stiffness using X-shaped mechanisms, *Mechanical Systems and Signal Processing* 170 (2022) 108267.
- [16] X. Huang, X. Liu, J. Sun, Z. Zhang, H. Hua, Vibration isolation characteristics of a nonlinear isolator using Euler buckled beam as negative stiffness corrector: a theoretical and experimental study, *Journal of Sound and Vibration* 333(4) (2014) 1132-1148.
- [17] B.A. Fulcher, D.W. Shahan, M.R. Haberman, C. Seepersad, P.S. Wilson, Analytical and experimental investigation of buckled beams as negative stiffness elements for passive vibration and shock isolation systems. *Journal of Vibration and Acoustics*, 136(3) (2014) 031009.
- [18] K. Kocak, C. Yilmaz, Design of a compliant lever-type passive vibration isolator with quasi-zero-stiffness mechanism, *Journal of Sound and Vibration* 558 (2023) 117758.

- [19] W. S. Robertson, M.R.F. Kidner, B.S. Cazzolato, A.C. Zander, Theoretical design parameters for a quasi-zero stiffness magnetic spring for vibration isolation, *Journal of Sound and Vibration*, 326(1-2) (2009) 88-103.
- [20] S. Yuan, Y. Sun, J. Zhao, K. Meng, M. Wang, H. Pu, Y. Peng, J. Luo, S. Xie, A tunable quasi-zero stiffness isolator based on a linear electromagnetic spring, *Journal of Sound and Vibration*, 482 (2020) 115449.
- [21] S. Sadeghi, S. Li, Fluidic origami cellular structure with asymmetric quasi-zero stiffness for low-frequency vibration isolation, *Smart Materials and Structures* 28(6) (2019) 065006.
- [22] P. Koutsogiannakis, D. Bigoni, F. Dal Corso, Double restabilization and design of force-displacement response of the extensible elastica with movable constraints, *European Journal of Mechanics-A/Solids* 100 (2023) 104745.
- [23] G. Gatti, An adjustable device to adaptively realise diverse nonlinear force-displacement characteristics, *Mechanical Systems and Signal Processing* 180 (2022) 109379.
- [24] S. Dalela, B. PS, D.P. Jena, M. Leblouba, A tunable metamaterial using a single beam element with quasi-zero-stiffness characteristics for low-frequency vibration isolation, *Journal of Vibration and Control* (2023) 10775463231198892.
- [25] Q. Zhang, D. Guo, G. Hu, Tailored mechanical metamaterials with programmable quasi-zero-stiffness features for full-band vibration isolation, *Advanced Functional Materials* 31(33) (2021) 2101428.
- [26] G. Gatti, Statics and dynamics of a nonlinear oscillator with quasi-zero stiffness behaviour for large deflections, *Communications in Nonlinear Science and Numerical Simulation* 83 (2020) 105143.
- [27] G. Yan, H.X. Zou, S. Wang, L. C. Zhao, Q. H. Gao, T. Tan, W. M. Zhang, Large stroke quasi-zero stiffness vibration isolator using three-link mechanism, *Journal of Sound and Vibration* 478 (2020) 115344.
- [28] P. Ling, L. Miao, B. Ye, J. You, W. Zhang, B. Yan, Ultra-low frequency vibration isolation of a novel click-beetle-inspired structure with large quasi-zero stiffness region, *Journal of Sound and Vibration* 558 (2023) 117756.
- [29] F. Zhao, J.C. Ji, K. Ye, Q. Luo, Increase of quasi-zero stiffness region using two pairs of oblique springs, *Mechanical Systems and Signal Processing* 144 (2020) 106975.
- [30] J. Bian, X. Jing, Analysis and design of a novel and compact X-structured vibration isolation mount (X-Mount) with wider quasi-zero-stiffness range, *Nonlinear Dynamics* 101(4) (2020) 2195-2222.
- [31] N.P. Mastrikola, R. Singh, Nonlinear load-deflection and stiffness characteristics of coned springs in four primary configurations, *Mechanism and Machine Theory* 116 (2017) 513-528.
- [32] A. Valeev, Dynamics of a group of quasi-zero stiffness vibration isolators with slightly different parameters, *Journal of Low Frequency Noise, Vibration and Active Control* 37.3 (2018) 640-653.
- [33] A.R. Valeev, A. N. Zotov, S. A. Kharisov, Application of disk springs for manufacturing vibration isolators with quasi-zero stiffness, *Chemical and Petroleum Engineering* 51 (2015) 194-200.
- [34] P. Gilmore, U Gandhi, Development of disc spring stack containment methods for vibration isolation, *INTER-NOISE 2021 Congress Proceedings* 263.2 (2021) 4871-4879.

[35] L.P. Hyatt, R.L. Harne, Programming metastable transition sequences in digital mechanical materials, *Extreme Mechanics Letters* 59 (2023) 101975.